Journal Pre-proof

Effects of baffle designs on damping acoustic oscillations in a solid rocket motor

Lei Han, Junwei Li, Dan Zhao, Xingpeng Gu, Baoyin Ma et al.

PII: S1270-9638(21)00337-0
DOI: https://doi.org/10.1016/j.ast.2021.106827
Reference: AESCTE 106827

To appear in: *Aerospace Science and Technology*

Received date: 23 May 2020
Revised date: 8 May 2021
Accepted date: 12 May 2021

Effects of Baffle Designs on Damping Acoustic Oscillations in a Solid Rocket Motor

Lei Han[a,b], Junwei Li[a, *], Dan Zhao[b], Xingpeng Gu[a], Baoyin Ma[a], Ningfei Wang[a]

[a] *School of Aerospace Engineering, Beijing Institute of Technology, Beijing 100081, China;*

[b] *Department of Mechanical Engineering, College of Engineering, University of Canterbury, Christchurch 8140, New Zealand*

Abstract

The baffle is a practical and promising passive damping method of dissipating acoustic energy and increasing acoustic losses in a solid rocket motor (SRM). In this study, numerical studies were conducted conjunction with the acoustic pulse response method (PRM) to evaluate the acoustic damping performance of a full-scale SRM with a baffle. The forced pulse function was imposed according to the frequency of the longitudinal acoustic mode. We comparatively evaluated the acoustic damping performance of the SRM with and without a baffle. The performances were characterized by (1) acoustic growth rate, (2) damping rate, and (3) acoustic energy. The PRM was first validated using data available in the literature. Several numerical investigations were conducted to develop geometry design criteria, which were subsequently used to ensure the effective operation of the baffle to suppress combustion-driven acoustic modes in the SRM. The effects of 1) the baffle axial location (x/L) and 2) the relative diameter (d/D) on acoustic damping performance were examined in detail. The results indicated that the baffle is effective in suppressing acoustic oscillations only when placed at 1/4 ≤x/L

[*] Prof. Junwei Li
School of Aerospace Engineering, Beijing Institute of Technology; E-mail: david78lee@gmail.com

≤1/2. Furthermore, when the baffle was placed at x/L=1/2, a relative improvement of approximately 51% and 15.3% in the growth and damping rates, respectively, was achieved compared with those in the SRM without a baffle. In addition, an annular baffle with a smaller inner diameter was observed to have a good design. A baffle with d/D=1/2 was observed to be associated with a favorable damping effect. This research elucidates the effective design of a baffle in stabilizing combustion in an SRM.

Key words: *Baffle; Acoustic damping; Solid rocket motor; Pulse response method; Damping rate; Acoustic energy*

1. **Introduction**

The problem of combustion instability in solid rocket motors (SRMs) is characterized by the presence of sustainable pressure oscillations in the chamber and thrust oscillations [1, 2]. Over the past decades, various SRMs (e.g., Reusable SRM, Engineering Test Motor, Titan SRM, P80 SRM, and Ariane 5 P230 SRM) have been reported to exhibit combustion instabilities during firing or cold flow test operations[3]. Such instabilities can result in apparent thrust oscillations and detrimental structural vibrations of the payload. This has attracted considerable interest [4-11] toward the exploration of suppressing mechanisms and solutions. The combustion instability of solid propellants results from amplification or attenuation of acoustic oscillations. Recent studies have revealed that unstable combustion is an effective acoustic source of generating acoustic pressure waves. These pressure waves propagate within the combustor, reflecting from the boundaries and back on the propellant surface [12], causing more time-dependent heat transfer and release. Thus, understanding the travel and growth of these acoustic waves is both fundamental to exploring the evolution of instability and the first step in seeking methods to improve the stability of the combustor [13].

Most of the research[14-16] on instabilities demonstrated that SRMs are primarily dominated by longitudinal acoustic oscillations, and motor design engineers were advised to implement the following available solutions [17, 18] to overcome the problem of combustion instability in SRMs: (1) change the grain configuration, (2) optimize the propellant formulation to either decrease the driving or increase the damping, and (3) add a mechanical suppression device to increase the damping[12]. The latter approach, the use of suppression devices, is the subject discussed herein. To dampen pressure oscillations, acoustic dampers (e.g., Helmholtz resonator, quarter-wavelength tube, perforated plate, and damping baffle) [19, 20] are widely applied as passive control methods to stabilize various combustion systems. For SRMs, both the quarter-wavelength tube and Helmholtz resonator exhibit a slight attenuation of the pressure oscillations and cannot be implemented on actual flights owing to their complex structure. Damping baffles are more practical in mitigating the longitudinal acoustic oscillation modes. A baffle is an annular structure located in a rocket chamber that dampens undesired oscillations. Helley [21] provided an invention to passively control pressure oscillations in a solid propellant by inserting a baffle to prevent instability. This method has been verified for practical applications in currently deployed motors.

For motors with a large aspect ratio that exhibit longitudinal instability, the damping baffle is generally employed as a passive control method for combustion instability [22]. This provides a possible control method to prevent or dampen the onset of pressure oscillations. Baffles can modify the acoustic resonance properties of the combustor without significantly altering its structure. Several experimental investigations with T-burners [23] and pulse guns [24] have been employed for the baffle to suppress acoustic modes. Extensive research [2] indicates that suppression baffles can be effectively used in solid propellant motors. The Von Karman Institute [3] conducted experimental studies, which demonstrated that metal baffles reduce pressure fluctuations in a satisfactory manner. This resulted in a net reduction of more than 48%. Full-scale or sub-scale tests generally require considerable time and cost to obtain the damping characteristics. Thus, a promising numerical method that is easily implemented and provides a quick answer for the damping performance of the baffle should be established.

The diameter of the baffle in the motor was also revealed to be important. The baffle is embedded within the propellant grain. As the firing progresses, the baffle becomes increasingly exposed. Consequently, the recommended baffle cross-section area (diameter) should be at the time of the worst instability onset. In addition, an inappropriate baffle location can fail to suppress the acoustic wave motion and associated motor performance loss. Severe heat transfer and pressure changes may cause the propellant to burn out prematurely in the aft segment. The aforementioned research confirmed that the implementation of a damping baffle can prevent or eliminate acoustic oscillations and result in a negative effect [25]. The location and geometry of the baffles are key factors in their design and installation, which significantly affects the optimum damping effect. However, detailed investigations on the optimum geometry criteria for baffles in motors are still insufficient. This partially motivated this study.

In this work, after exciting acoustic oscillation by superimposing a dominated acoustic pulse on the mass flow rate by user-defined function (UDF) at the head-end of the combustor, the frame of pulse response method is used to quantitatively study on the damping effect of the baffle in the solid rocket motor. The damping effect of baffle on the stability of the solid rocket motor performance has two aspects: a) suppression on pulse growth, b) synergy on pulse decay. With the present state of the art, the primary issue is represented by the capability in evaluating the damping characteristics of the in-duct baffle damper in SRM port, in terms of growth rate, damping rate, and acoustic energy[26].

A comprehensive quantitative analysis of the damping effect in SRMs is considered mandatory in providing a detailed scenario on the exact function of an annular baffle. A series of numerical studies were conducted to develop evaluation methods and geometry design criteria that may be used to ensure effective operational use of baffles to suppress acoustic modes of combustion instability in solid propellant motors. The acoustic growth and damping rates of motors with and without a baffle were compared. Analyses of the acoustic energy budget and phase diagram were also used to evaluate the respective contributions of the baffle to pulse growth and pulse attenuation. A two-dimensional (2D) axisymmetric model of a solid propellant motor is presented in Section 2.1. The numerical method and boundary conditions are described in Sections 2.2 and 2.3. The model verifications and grid dependency test are presented in Section 2.4. Comprehensive quantitative analyses are finally conducted in Section 3 to explore the effect of two key parameters: the baffle axial location (x/L) and relative diameter (d/D). The main conclusions of the baffle design criteria and the optimum outcomes are summarized in Section 4.

2. Theoretical Foundation and Computational Methods

2.1Numerical Models and Parameters

In SRMs, the internal flow is composed of streamlines ejected from the surface of a burning propellant that turn and travel in the longitudinal direction. A schematic of the aft-finocyl SRM at end of the burning is shown in Fig. 1. The distance from the head to nozzle throat is the total length (L). The inner diameter and outer diameter of the annular baffle are d and D respectively. The installation location of the baffle is defined as x. The object of study was a large-aspect-ratio ($x/L > 10$) [27] SRM with an aft-finocyl grain. This type of SRM is prone to suffer from first longitudinal acoustic instability at the end of its operation time [28]. The baffle is embedded within the propellant grain and will become increasingly exposed as the propellant burns.

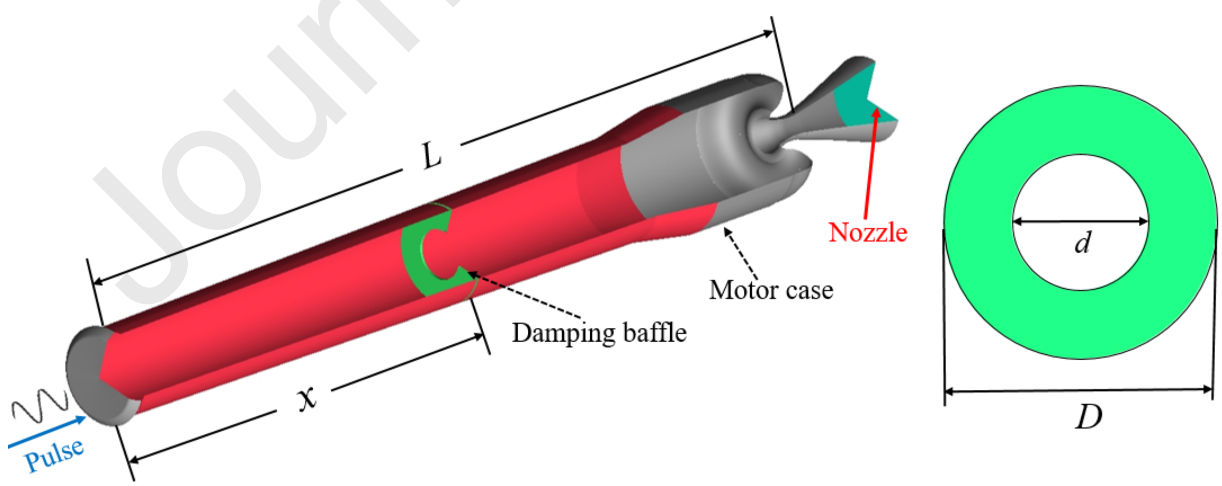

Fig. 1 Physical model scheme

The computational domain was simplified to a 2D axisymmetric model. Therefore, the baffle location and diameter were the dominant geometric parameters affecting the suppression of combustion instability. Fig. 2 shows the baffle location and acoustic mode. The ten cases listed in Table 1 were numerically studied to explore the geometry of the baffle on the damping effect. For comparison, case 0 was considered a baseline motor without a baffle. The operating conditions of all the cases were the same to facilitate comparison.

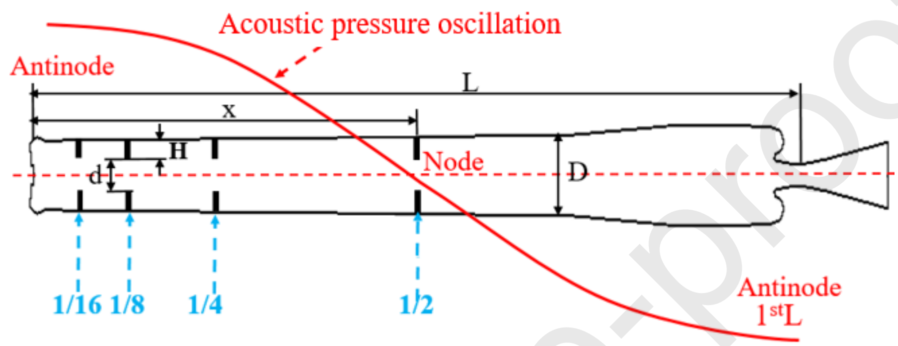

Fig. 2 Computational model scheme and baffle locations

Table 1. Baffle geometries of all cases

Case	Location (x/L)	Diameter (d/D)	Porosity (%)	Remark
Case-0	–	–	100	Without baffle-(2D)
Case-0-3D	–	–	100	Without baffle-(3D)
Case-1	1/16	1/2	25	1/16L-1/2D
Case-2	1/8	1/2	25	1/8L-1/2D
Case-3	1/4	1/2	25	1/4L-1/2D
Case-4	1/2	1/2	25	1/2L-1/2D
Case-5	1/4	5/8	39	1/4L-5/8D
Case-6	1/4	3/4	56	1/4L-3/4D
Case-7	1/4	7/8	77	1/4L-7/8D
Case-8	1/4	15/16	88	1/4L-15/16D

This SRM was filled with an AP/hydroxyl-terminated polybutadiene (HTPB) four-component propellant, and its operating pressure was greater than 11 MPa in the ground test. The detailed formulations of the HTPB propellant are listed in Table 2. With this propellant, the SRM from Fig. 1 was observed to experience pressure oscillations at the end of burning. This was the background and motivation for this research in exploring the optimum structural parameters of the baffle.

Table 2. Detailed formulations of HTPB propellant

Component	AP	HTPB	RDX	Al
Amount (wt.)	51%	10%	21%	18%

The specific physical parameters were calculated using thermodynamics software CEA [29] as the input for the numerical simulation, and they are listed in Table 3. The gas was assumed to be ideal, with its viscosity fitted by the Sutherland function at different temperatures.

Table 3. Physical properties of gas for numerical simulation

Parameters	Value
Constant-pressure specific heat (C_p)	*2046* J/kg·K
Specific heat ratio of gas (γ)	*1.16223*
Total Temperature (T)	*3532* K
Density (ρ)	Ideal gas
Dynamic viscosity (μ)	Sutherland law
Gas constant (R)	*415.1* J/kg·K
Molar mass (M)	*29* kg/kmol

2.2Numerical Method

In this study, numerical analysis was performed using the commercial computational fluid dynamics (CFD) platform ANSYS Fluent 19.2, which has been successfully used for simulations in the acoustic field [4, 30]. The RNG k–ε turbulence model with scalable wall functions was employed to solve the Navier–Stokes equations. This approach simultaneously solves the governing equations of continuity, momentum, and energy. When chemical reactions are neglected, these equations can be expressed in the following conservative form [31]:

$$\frac{\partial \rho}{\partial t} + \frac{\partial(\rho u_i)}{\partial x_i} = 0 \tag{1}$$

$$\frac{\partial(\rho u_i)}{\partial t} + \frac{\partial(\rho u_i u_j)}{\partial x_j} = -\frac{\partial p}{\partial x_i} + \frac{\partial}{\partial x_j}\tau_{ij} \tag{2}$$

$$\frac{\partial}{\partial t}\left[\rho\left(e + \frac{V^2}{2}\right)\right] + \frac{\partial}{\partial x_j}\left[\rho u_j\left(e + \frac{V^2}{2}\right) + p + q_j\,\partial u_i \tau_{ij}\right] = 0 \tag{3}$$

where u is the instantaneous velocity, V is the velocity modulus, p is the pressure, ρ is the fluid density, q_j is the heat flux, and τ_{ij} is the viscous stress tensor.

The coefficient of turbulent viscosity μ_t are calculated from turbulence kinetic energy k and turbulence dissipation rate ε. The transport equation for the standard k−ε model is shown as follows:

$$\frac{\partial}{\partial t}(\rho k) + \frac{\partial}{\partial x_i}(\rho k u_i) = \frac{\partial}{\partial x_j}\left(\alpha_k \mu_{eff} \frac{\partial k}{\partial x_j}\right) + G_k + G_b - \rho\varepsilon - Y_M + S_k \tag{4}$$

$$\frac{\partial}{\partial t}(\rho\varepsilon) + \frac{\partial}{\partial x_i}(\rho\varepsilon u_i) = \frac{\partial}{\partial x_j}\left(\alpha_\varepsilon \mu_{eff} \frac{\partial \varepsilon}{\partial x_j}\right) + C_{1\varepsilon}\frac{\varepsilon}{k}(G_k + C_{3\varepsilon}G_b) - C_{2\varepsilon}\rho\frac{\varepsilon^2}{k} - R_\varepsilon + S_\varepsilon \tag{5}$$

In these equations, G_k represents the generation of turbulence kinetic energy due to the mean velocity gradients. G_b is the generation of turbulence kinetic energy due to buoyancy. Y_M represents the contribution of the fluctuating dilatation in compressible turbulence to the overall dissipation rate. The quantities α_k and α_ε are the inverse effective Prandtl numbers for k and ε, respectively. S_k and S_ε are user-defined source terms.

The scale elimination procedure in the RNG theory results in a differential equation for the turbulent viscosity:

$$d\left(\frac{\rho^2 k}{\sqrt{\varepsilon\mu}}\right) = 1.72\frac{\hat{v}}{\sqrt{\hat{v}^3 - 1 + C_v}}d\hat{v} \tag{6}$$

$$\hat{v} = \frac{\mu_{eff}}{\mu} \quad (7)$$

$$C_v \approx 100 \quad (8)$$

Equation (6) was integrated to obtain an accurate description of the variation of effective turbulent transport with the effective Reynolds number, enabling the model to better manage low-Reynolds number and near-wall flows.

In the high-Reynolds number limit, Equation (6) yields

$$\mu_t = \rho C_\mu \frac{k^2}{\varepsilon} \quad (9)$$

with $C_\mu = 0.0845$, derived using RNG theory. This value of C_μ used in the standard model is very close to the empirically determined value of 0.09.

Scalable wall functions were used to impose the usage of the log law in conjunction with the standard wall function approach [31]. All y* values for wall cells were larger than 11.225. The second-order implicit formulation was used in an unsteady solver for the mass and momentum equations. The Courante–Friedriche–Lewy number was set to 1 and the time step was 5×10^{-5} s to achieve the evolution of acoustic pressure fluctuations. For the simulation, numerical convergence was achieved by satisfying the following two requirements: First, the pressure oscillation amplitude should be kept nearly constant as the number of iterations increases. Second, the mass flow rate imbalance between the inlet and outlet should be monitored until it reaches a small value (10^{-4}–10^{-5} kg/s) [32].

Boundary Conditions:

The essential boundary conditions of computational fluid dynamics (CFD) at the head, nozzle exit, and walls are set as follows:

Head: The mass flow rate in the motor is a function of pressure. The equation was as follows derived from Ref. [33]: $\dot{m} = C_D P_c A_t = \frac{\Gamma}{\sqrt{RT_f}} P_c A_t$, where C_D is the mass flow rate coefficient, P_c is the equilibrium pressure in the chamber, A_t is the throat area of nozzle, Γ is the parameter related to the specific heat ratio, and T_f is the adiabatic combustion temperature. Acoustic pulse is stimulated by injecting gas at the unsteady mass flow inlet, the gas total temperature is 3532K, the flow rate of which is defined as $\dot{m} = |\bar{m}|\left[1 + \left|\frac{m'}{\bar{m}}\right| \cdot \sin(\omega t + \theta_0)\right]$,

where $\bar{m}$ and m' are the mean mass flow rate and amplitude of the pulse, respectively. $\omega=2\pi f$ denotes the pulse frequency, θ_0 is phase angle.

Nozzle exit: Pressure outlet boundary condition with 1.01325×10^5Pa and 298K were assumed where the quantities were extrapolated from the flow variables within the cells of the upstream computational domain

Motor case: The wall boundary condition was adopted as an adiabatic no-slip condition.

Six virtual pressure monitors were set along the axial direction to record the pressure change history. The detailed locations of the monitors are listed in Table 4.

Table 4. Detailed normalized locations of monitors

Monitors	P_0	P_1	P_2	P_3	P_4	P_5
$(\frac{x}{L}, \frac{y}{D/2})$	(0, 0)	(1/16, 0)	(2/16, 0)	(3/16, 0)	(4/16, 0)	(5/16, 0)

2.3 Pulse Response Method (PRM)

Extensive research [34, 35]has been performed to apply the linear instability theory to the prediction of the stability of SRMs. In practice, different SRMs must satisfy different stability requirements during different operation scenarios. The numerical simulation process using the pulse response method (PRM) is shown in Fig.3. The upper curve is the chamber response, and the lower trace is the pulse function. The damping effect of the baffle on the stability performance of the SRM has two aspects: (a) suppression of pulse growth and (b) attenuation of pulse decay. Suppression of the trigger pulse means that the baffle (or any other structure in the motor) can suppress the evolution or weaken the perturbation growth of the pulse when an external trigger pulse disturbance occurs abruptly. If a motor remains continuously unstable after a pulse, the mitigation of the steady pulse is the damping effect of the baffle that the acoustic oscillation dissipates to reduce its effect on motor operation. An unstable motor will inevitably return to a stable state when its pressure is not divergent or unlimited. The synergy of the attenuation pulse is the effect of the damping baffle to promote acoustic oscillation dissipation and attenuation in the stage of an unstable motor back to a stable state.

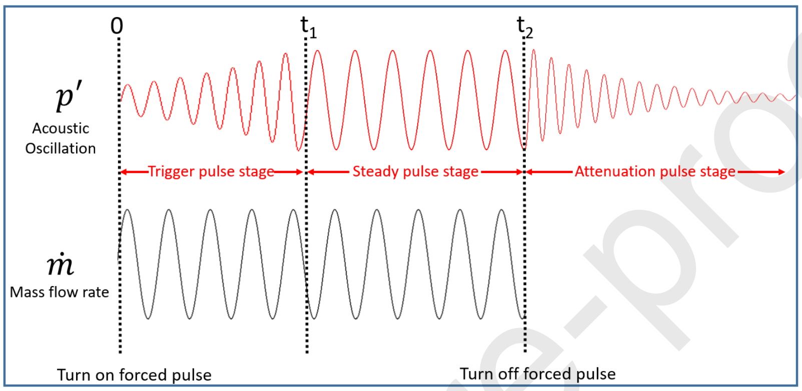

Fig. 3 Process of pulse response method

The PRM was effectively used to evaluate the nozzle damping coefficient in experiments at the U.S. Naval Ordnance Test Station [14, 24]. In this study, the PRM was a numerical method developed by considering both the growth and damping rates of acoustic pressure oscillation and applied to the damping evaluation of the baffle. Generally, an unstable motor with an operation pressure (p) indicates that

$$p = \overline{p} + p'(t) \tag{10}$$

where $\overline{p}$ is the average pressure, and $p'(t)$ is the acoustic pressure oscillation. Solid rocket motor instability is the amplification or attenuation of acoustic oscillations caused by solid propellant combustion processes in the chamber. Therefore, the coefficients α_{GR} and α_{DR} are representatives of amplification or attenuation performance that sum the driving and damping terms, including pressure coupling, velocity coupling, nozzle damping, and structure damping. We assumed that a motor chamber only affiliated with a baffle has no additional dissipation of acoustic energy. Therefore, the acoustic oscillation is not damped by factors other than the baffle itself. The amplitude of the acoustic oscillations increases linearly. Therefore, the growth rate of the acoustic oscillation amplitude is expressed as

$$\alpha_{GR} = \frac{p'(t_2) - p'(t_1)}{t_2 - t_1} \tag{11}$$

When the forcing acoustic oscillation pressure signal is turned off, the baffle damping effect is determined by the damping rate. Under these conditions, the evolution of the acoustic pressure amplitude of the combustor can be represented as an exponential [14, 36]. This can be illustrated by the following equation:

$$p'(t) = p_0 \sin(\omega, t) e^{\alpha_{DR} t} \tag{12}$$

where p_0 is the initial amplitude, t is the time evolution, and ω is the oscillation frequency. In this study, α_{DR} was used only for the baffle damping performance was proposed without considering the combustion kinetics. According to Eq. (9), the amplitude of the acoustic pressure oscillation decays exponentially. Therefore, the damping rate can be obtained by plotting the peak-to-peak amplitude–time profile in a logarithmic time coordinate system to quantify the damping effect of the baffle:

$$\alpha_{DR} = \frac{\ln p'(t_2) - \ln p'(t_1)}{t_2 - t_1} \tag{13}$$

To facilitate the application of the pulse response method [37] in this research, a periodic pressure oscillation signal with a frequency equivalent to the first longitudinal acoustic mode was imposed on an unsteady flow at the head end of the chamber via UDF for 1.0 s to obtain the growth rate and acoustic energy budget, and the damping rate was obtained when the pressure oscillation was turned off.

The instantaneous acoustic energy ($E_a(t)$) evolution for oscillation ($p'(t)$) can also be used to quantify the damping effect of the baffle [38] [12]. The acoustic energy of every unit volume of the chamber is defined as [39]:

$$E_{\mathrm{a}}(t)=\frac{\frac{\omega}{2\pi}\int_{t}^{t+2\pi/\omega}\left[p'(t)\right]^{2}\mathrm{d}t}{2\gamma p_{0}} \tag{14}$$

where ω is the oscillation frequency, $p'(t)$ is the acoustic pressure fluctuation, $\gamma = 1.16$ is the specific heat ratio, and p_0 is the mean atmospheric pressure.

$$E_{\mathrm{a}}^{\mathrm{tot}}(t)=\int_{0}^{2\pi}\mathrm{d}\vartheta\int_{0}^{R}r\mathrm{d}r\int_{0}^{L}E_{\mathrm{a}}(t)\mathrm{d}x \tag{15}$$

Pulse amplitude (or intensity) and frequency are the two main factors that impose pulse pressure oscillation signals in the PRM. The frequency is determined by the first longitudinal acoustic oscillation frequency calculated using classical acoustic theory [40]. In this study, longitudinal oscillation was of primary concern. According to classical acoustic theory, the longitudinal acoustic mode frequencies of the motor can be expressed as follows:

$$f_n = na/2L = n\cdot\sqrt{\gamma RT}/2L \tag{16}$$

where n=1, 2, 3… is the acoustic mode, L is the length of the closed-closed cylinder, T is the temperature and R is the gas constant.

2.4 Model Verifications and Grid Dependency Test

2.4.1 Applicability of 2D simplification

Three-dimensional (3D) and 2D simulations were first conducted to verify the applicability of the 2D axisymmetric model. We set the time step as 5e-5 s, the mesh element as 20 million, and unsteady time up to 1 s. The computations were performed over 64 thousand core-hours (AMD EPYC 7452, Linux 64 bit). The results of the 2D and 3D simulations were compared to illustrate the rationality of 2D simplification. Fig. 4 depicts the normalized acoustic pressure distribution based on the 2D and 3D calculation results. The contours of the acoustic pressure were consistent.

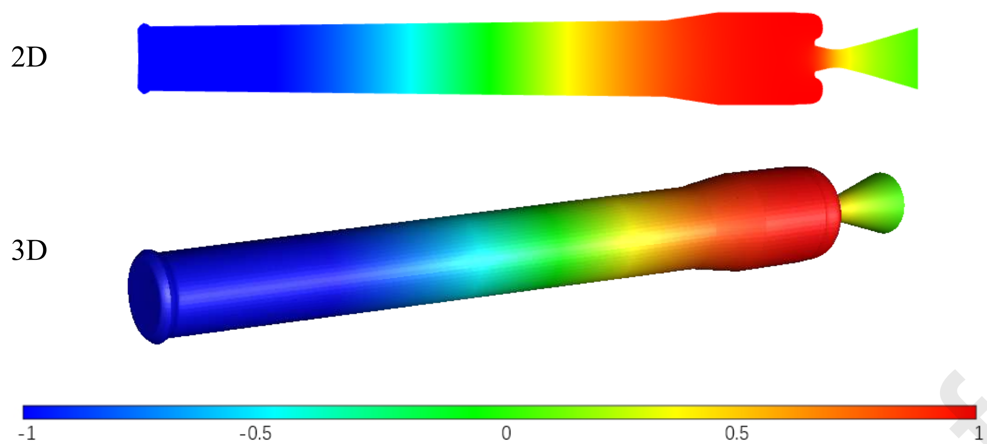

Fig. 4 Comparison of the normalized acoustic pressure distribution of 2D and 3D models.

We compared the parameters of acoustic pressure characteristics. The change in the acoustic pressure with time is shown in Fig. 5 (a). The acoustic oscillation frequencies and amplitudes of the corresponding limit cycles are compared in Fig. 5 (b). We observed that the oscillation frequency of the 3D model was exactly the same as that of 2D model (159 Hz). The relative deviation of the limit cycle amplitude was no more than 7%. For the convenience of comparison, the limit cycle and decay zones are magnified in Fig. 5 (c) and (d). The details of the acoustic pressure evolution and decay process were consistent in both the 2D and 3D models. This indicates that the 2D model used in this study can be used as an effective substitute for the 3D model when considering computational cost and efficiency.

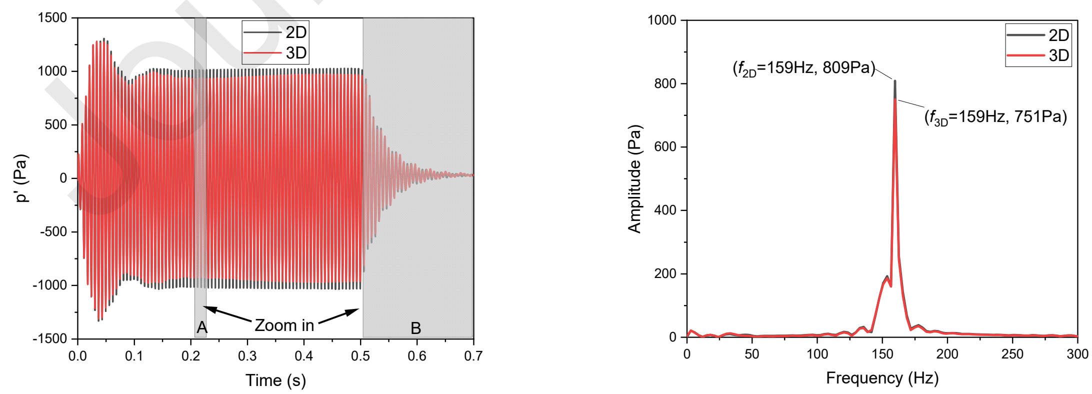

(a) Acoustic pressure evolution **(b) FFT of limit cycle**

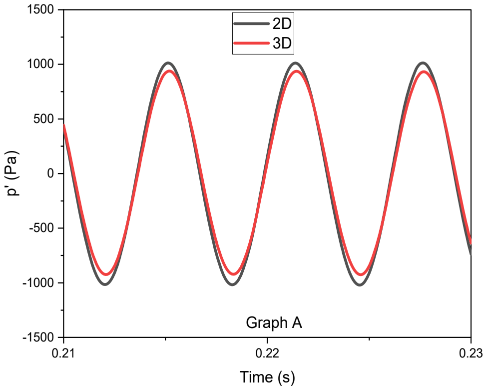

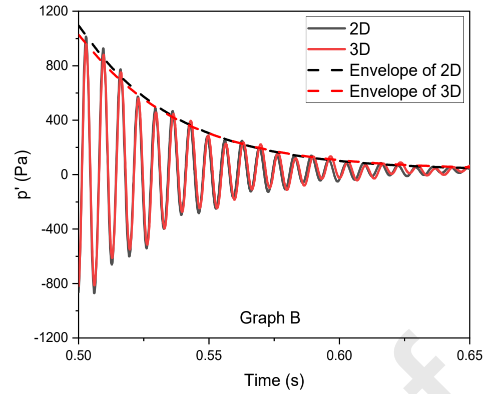

(c) Zoom in graph A **(d) Zoom in graph B**

Fig. 5 Comparison of 2D and 3D model

2.4.2 Grid Dependency Test

Grid dependence test was performed in two steps to guarantee that the selected mesh density was suitable for the prescribed turbulence closure model. The evolutions of the pressure values in the first step are compared in Fig. 6, where the other parameters were kept constant. The coarsest mesh with 60 k had approximately 60 thousand cells, and the finest grid had 960 thousand cells. Five grids with a ratio of 1:2:4:8:16 were studied. The pressures of the 60 k and 130 k grids did not fit well, particularly at the peak value of the limit cycle. The results indicated good consistency when the grid was higher than 240 thousand cells (240 k). This grid was employed for all the subsequent numerical computation because it had an excellent trade-off between computational accuracy and time cost. Furthermore, the corresponding grid size was selected in the geometrical models with different baffle implementations.

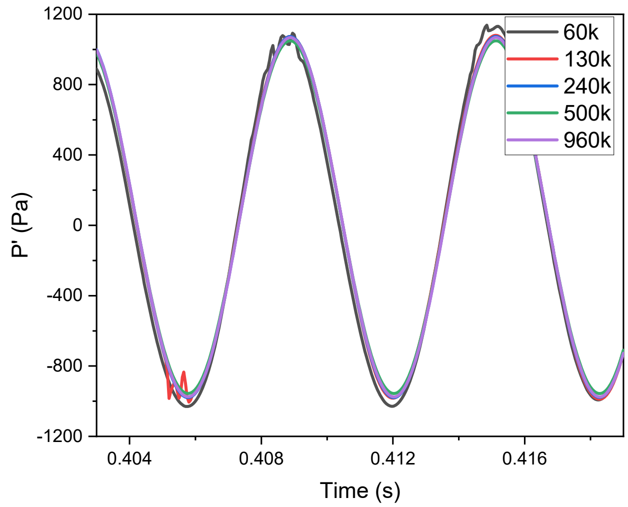

Fig. 6 Comparison of mesh independence

The second step is to carry out a grid independence study on the damping ratio. Damping coefficients under different grid scales are compared. It can be seen that when the mesh number is greater than 500K, the damping coefficient almost remains unchanged. The difference between the value at 240K grid-scale and that at 500K grid-scale is only 0.009.

The grid convergence index (GCI) [41] was analyzed to quantitatively evaluate grid convergence.

$$GCI = \frac{F_s \left| \frac{(f_2 - f_1)}{f_1} \right|}{r^p - 1} \tag{17}$$

Here, f is the parameter selected for the convergence. In this study, it was the damping ratio. Subscripts 1 and 2 correspond to the fine and selected grids, respectively. The values of F_s=1.25, r=2, and p=2, as suggested by Roache [41]. The maximum error between the mesh with 240 k and 500 k cells was approximately within 0.14%. This analysis indicated that the grid was adequate to capture most of the features of the flow, and the solution was grid-independent. The mesh with 240 k cells was selected for all the subsequent numerical computations because it created an excellent trade-off between computational accuracy and time cost.

2.4.2 Temporal convergence study

To check the temporal convergence, we fixed the mesh size at 250K such that the error from the spatial discretization is negligible compared to the time stepping error. The increasing time step size 5e-5, 2.5e-4 and 1.25e-3 s are chosen to run the simulation up to 1s. The temporal convergences of acoustic oscillation pressure are depicted in Fig.7. It can be observed that the convergence is in good agreement when time step below 2.5e-4 s.

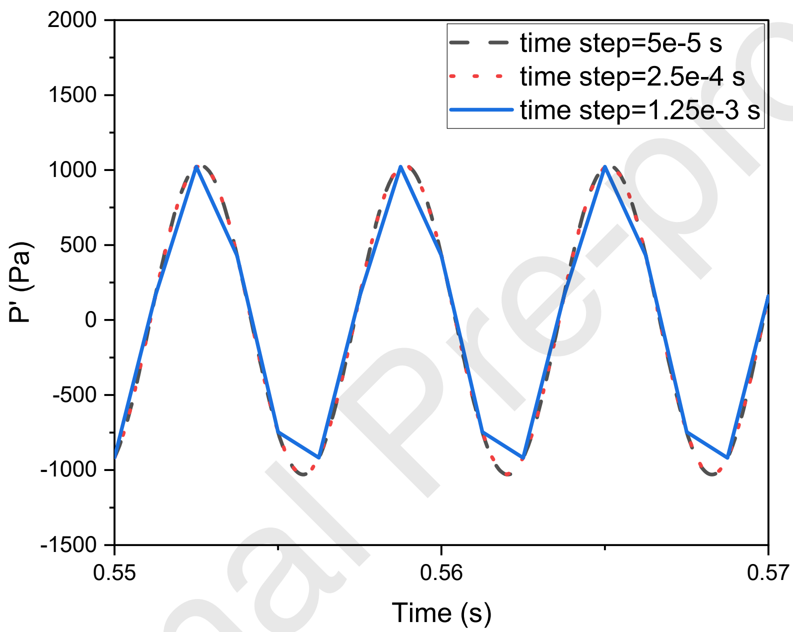

Fig.7 Temporal convergence study

To ensure the accuracy of the numerical method and grid-scale calculation adopted in this study, we compared the numerical results with the results of Buffum [24] to evaluate the reliability of the numerical scheme. Buffum [24] and Sun [4] conducted research on the nozzle damping rate based on this tester. Fig. 8 shows the damping rates of the nozzle from both Ref. [4] and our simulations. These results were observed to be considerably consistent, including the trend of distribution and the values.

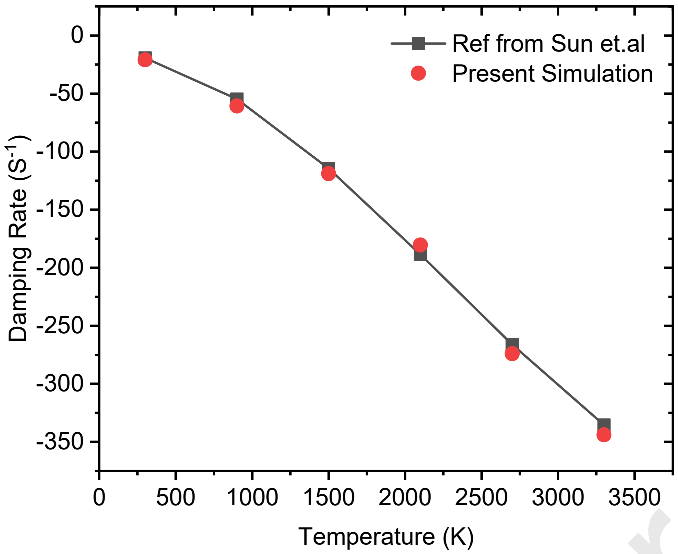

Fig. 8 Comparisons of damping rate from Ref. [4] and present simulation data

The pulse amplitude has a significant effect on combustion instability. Generally, the larger the pulse intensity, the more easily the combustion instability can be excited [2]. The decay process of pressure oscillation under different pulse amplitude conditions of the numerical simulation and experimental test are provided in Ref. [14]. The pressure decay rate at different pulse intensities in the experimental test and numerical simulations were observed to remain basically unchanged, that is, the damping coefficients of the experimental and numerical data were almost the same under different pulse intensity conditions. The damping rate was verified for all numerical and experimental cases and was observed to be independent of the pulse amplitude. In addition, these results were well validated by the theoretical simulation results in Ref. [37].

3. Results and Discussion

3.1 Effect of the Baffle on Acoustic Field Characteristics

Numerical simulations using the method presented in this manuscript were first conducted to analyze the physical mechanisms occurring in the vicinity of the baffle when acoustic waves impinge on it. Fig. 9 shows the instantaneous acoustic pressure contours of the two scenarios for an entire oscillation period. The divergence part of the nozzle is omitted because it did not affect the acoustic field in the combustor. If the first-order axial oscillation occurs in the combustor, the waves propagate within the motor and generate a steady oscillation. According to classical acoustic theory [31], a motor with closed ends has acoustic pressure anti-nodes at both ends. The acoustic field here completely corresponded to this, which indicated that the method adopted can effectively excite the required oscillation. The acoustic field was excited and exhibited the characteristics of acoustic standing waves. The absolute acoustic pressure at the head and bottom ends of the motor initially decreased and then increased. The absolute acoustic pressure was most intense at both ends of the chamber. The absolute acoustic pressure at the mid-point of the motor was the weakest compared with the other positions. The oscillation amplitude level in the motor with the baffle was much smaller than that of the motor without one. Because the same color scale was used, the banded contour was present in the motor with the baffle owing to the lower range. This indicated that the adopted baffle was sensitive to the acoustic pressure oscillation of the first acoustic mode.

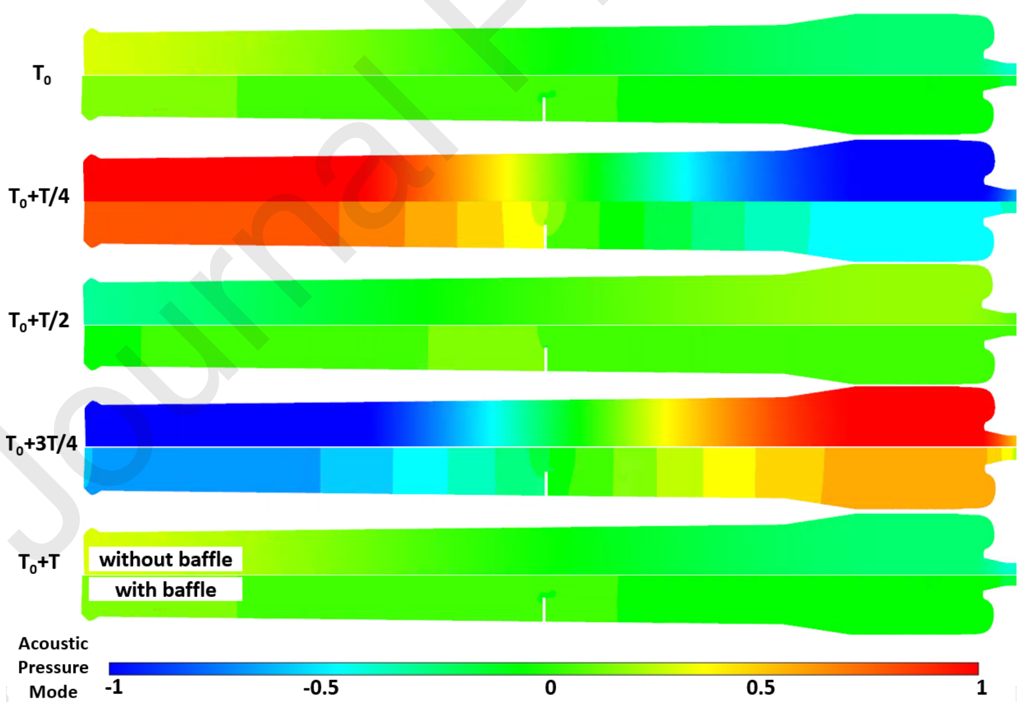

Fig. 9 Comparison of acoustic pressure mode of the SRM with or without the baffle (case 4 and case 0)

The comparisons of the acoustic wave pressure shape evolution over the entire period are shown in Fig. 10. The light gray zone is the location of the baffle in case 4. We can conclude that both motors in cases 0 and 4 successfully simulated the first mode acoustic modes. This was consistent with the results shown in Fig. 9. The acoustic pressure shapes were the same during the different time periods. The head and end of the motor were acoustic pressure anti-nodes that achieved the maximum magnitude. The anti-node amplitude of the motor with the baffle was only half that of the reference motor. The mid-point amplitude of the motor was always maintained at zero, which corresponded to a pressure node. This was because the acoustic pressure amplitude was always zero at the baffle position; therefore, the suppression effect was reflected only at both ends of the motor. However, the acoustic pressure oscillation distribution amplitude along the axial direction was smaller when a baffle was in the motor. This indicated that the acoustic pressure mode of the modeled combustor was affected by the baffle. It only affected the acoustic amplitude but not the mode shape.

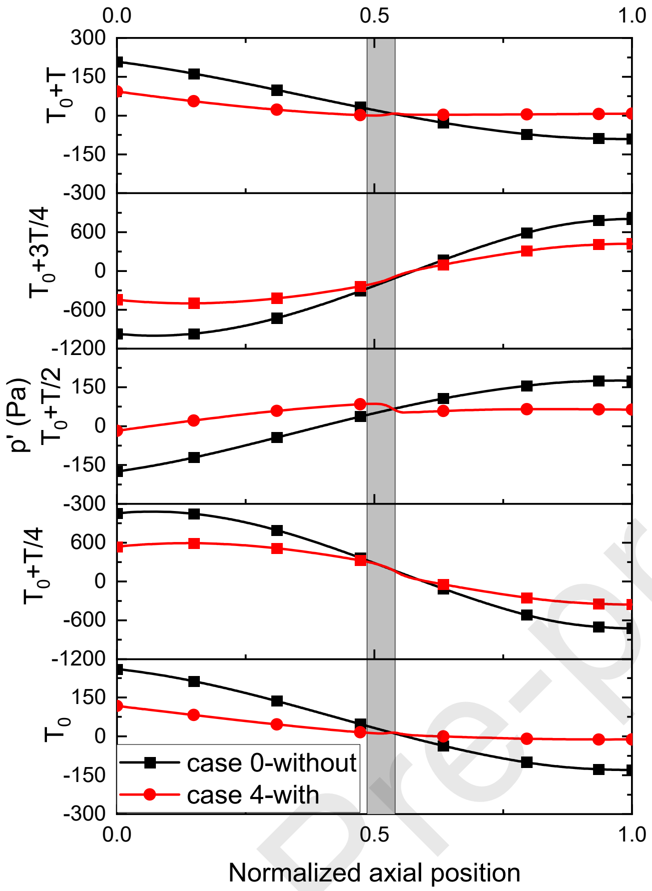

Fig. 10 Comparison of acoustic pressure shape evolution in period *T* of the SRM with and without a baffle. (The grey area is the baffle location in case 4)

Fig. 11 compares the evolution of contours on the normalized acoustic velocity mode of the two motors in the absence and presence of the baffle. The acoustic velocity at the head and bottom ends of the motor initially increased at T_0 and then decreased over the phase angle. The velocity anti-node was located in the middle of the chamber, where the acoustic velocity was the highest all-time compared with the other positions. The acoustic velocity nodes were located at the head and end of the motor. However, when the acoustic disturbance was assumed to be unchanged from the pulse, the baffle dramatically changed the local velocity shape, particularly in the middle region of the motor. This was because the baffle reduced the flow passage area. It had an apparent effect on the local acoustic velocity mode at the baffle location, but not at the ends of the motor. It represented the acoustic energy dissipation due to the damping resulting from the baffle in the acoustic viscous and flow shear layers at the tip of the baffle.

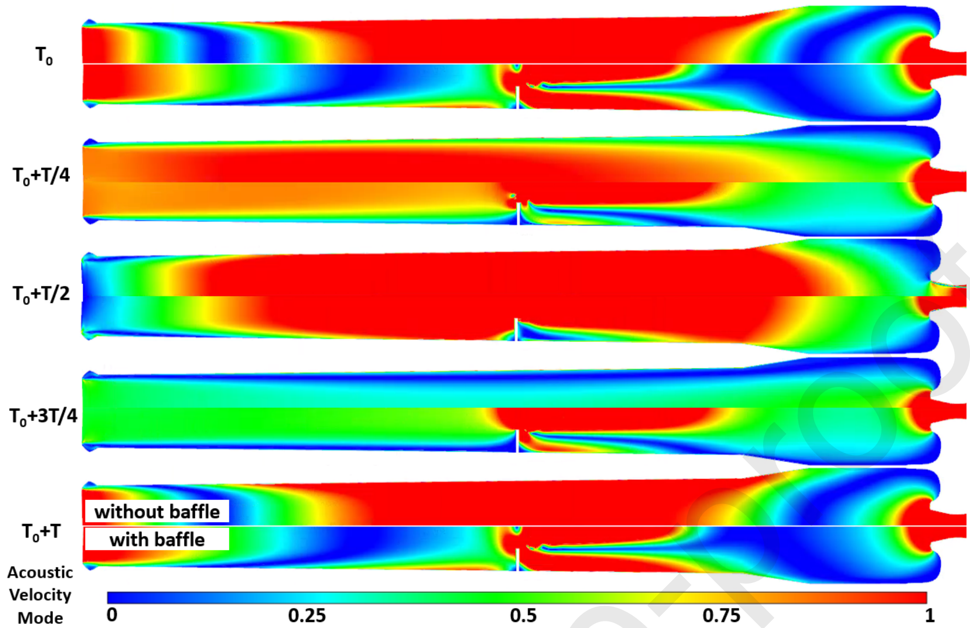

Fig. 11 Comparison of acoustic velocity oscillation mode of the SRM with baffle or without (case 4 and case 0)

Fig.12 compares the profiles of the acoustic velocity mode in the axial direction at a different time for the motors with and without a baffle. The acoustic velocity mode shape for the motor without a baffle was symmetrical. From the head to the end of the case 0 motor, the acoustic velocities increased gradually and then decreased. The head and end of the motor were the acoustic velocity nodes. The mid-point of the motor was the acoustic velocity anti-node, which achieved the maximum acoustic magnitude. The acoustic velocity profile with the same convex shape as the first mode depicts. The most distinct difference was that the maximum acoustic velocity increased abruptly after the baffle was implemented. A peak was observed to be located behind the baffle. However, the acoustic velocity amplitude at the axial line was also smaller when the baffle was in the motor. The baffle was more sensitive to the magnitude of the acoustic velocity than to the acoustic pressure. In summary, the baffle at the maximum acoustic velocity (anti-node) and minimum acoustic pressure (node) operated effectively by dissipating more acoustic energy, but for the extent of the specific effect, the damping performance required further analysis, which is described in the following section.

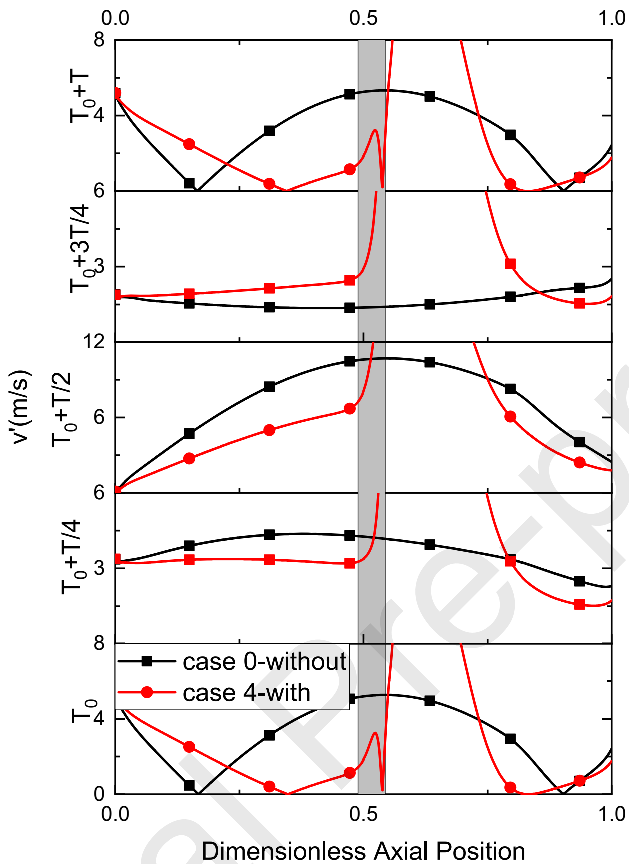

Fig. 12 Acoustic velocity oscillation evolution in the SRM with and without baffle (The grey area is the baffle location in case 4)

The internal flow field that passes through a baffle separates as a core flow, constituting a continuous source of vorticity produced within the jet shear layers. When acoustic waves interact with the jet, a fraction of the acoustic energy of the incident acoustic wave is converted into vortical energy, which is eventually dissipated by viscous losses [42]. The dissipation of acoustic energy is proportional to the viscous losses from the vorticity of the baffle edges. The turbulent viscosity ratio is a significant symbol of turbulent viscosity loss. A more intense turbulent viscosity indicates that acoustic energy is easily converted into vortical energy and dissipated without significant acoustic regeneration [43]. Fig.

13 shows a comparison of the turbulent viscosity ratio of the motor flow field with and without an in-duct baffle, as the baffle location was set to 1/2 and the first longitudinal oscillation occurred. The monitor line position is located at downstream and close to baffle. The data in the figure of that area is zoomed for comparison. Most of the turbulent viscosity ratio along the radial direction was higher when the baffle was in the motor. The baffle changed the local viscosity dramatically, particularly in the edge region of the baffle. The turbulence caused by the viscosity enhanced the conversion between the acoustic wave and vortical energy

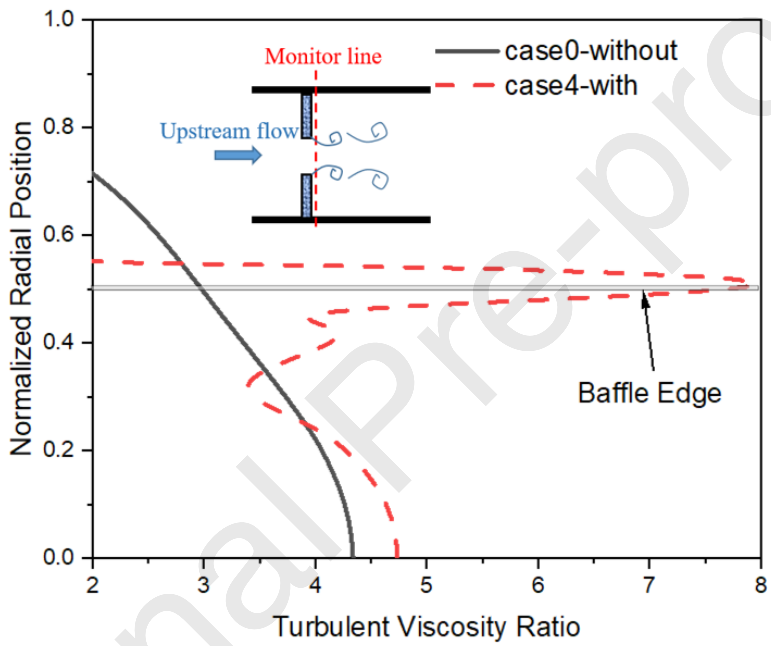

Fig. 13 Dramatic change of turbulent viscosity ratio of the motor with or without baffle of 1/2 location

3.2 Effect of Baffle on Damping Performances

Section 3.1 discusses the acoustic field under the entire periodic simulation. In this section, the damping of the baffle is quantitatively analyzed, and the processes of pulse growth and pulse attenuation are analyzed. An acoustic forcing pulse is triggered by imposing a small harmonic mass rate at the head end, which eventually sets a standing wave on the first axial acoustic mode with a small non-dimensional pressure amplitude. An acoustic pulse imposed at 0 s was used to evaluate the effect of the baffle on suppressing the trigger pulse pressure oscillation. The suppressing effect of the baffle on the trigger pulse was measured by calculating the growth rate to quantify the damping. Fig. 14 (a) compares the time evolution of the acoustic pressure fluctuations at the head of case 0 (without baffle) or case 4 (with baffle at x/L=1/2), as the baffle was set at the midpoint of the chamber. Small-amplitude pressure disturbances initially occurred and then gradually increased into a steady cycle pressure. The growth rate was used to quantify the damping performance of the trigger pulse. The growth rate after the trigger pulse can be obtained by plotting the peak-to-peak acoustic oscillation amplitude-time curve (Fig. 14 (a)). After linear fitting, we observed that the growth rate decreased from 40248 to 24254 Pa/s owing to baffle implementation. The growth rate of the improved motor was only 60% of that of the original motor. We observed that the optimized result of the growth rate was nearly equivalent to the acoustic pressure amplitude. The baffle was observed to have a greater damping effect than the original motor.

The forced acoustic pulse was stopped at t=1.00 s with a controlled mass flow rate to evaluate the effect of the baffle on the attenuation of pulse oscillations. Note that the simulations only provided the total damping rate of a motor with or without a baffle. Fig. 14 (b) shows the time evolutions of the numerical acoustic pressure signal fluctuations at the head end of the combustors decay with an exponential rate of t>1.00 s. The dashed line is an exponential fit that enabled us to determine the damping rate. We observed that the steady disturbances gradually decayed into a small-amplitude pressure oscillation.

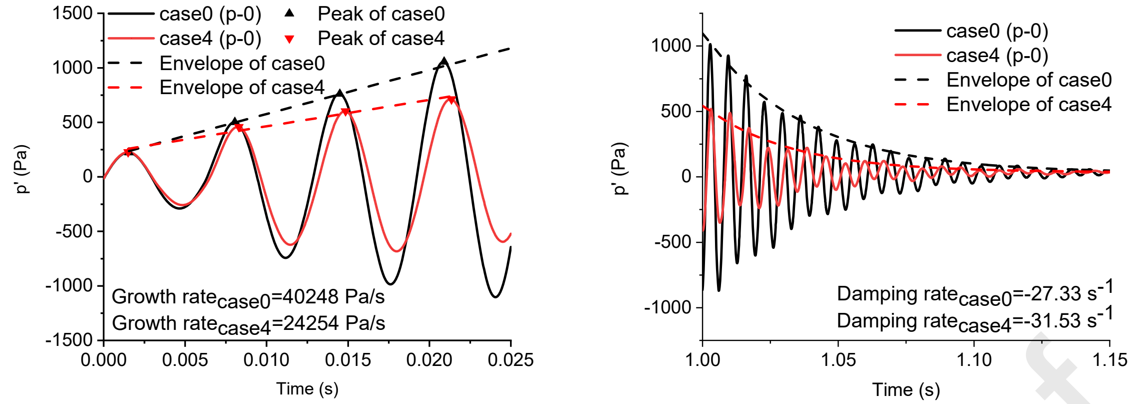

(a) **Growth of acoustic oscillation** (b) **Decay of acoustic oscillation**

Fig. 14 Acoustic oscillation response. Forcing pulse was begun at t=0 and stopped at t=1.00 s. The dashed line is an envelope of linear or exponential fit.

The damping rate was used to quantify the damping performance of the attenuation pulse. The damping rate could also be obtained by plotting the peak-to-peak acoustic oscillation amplitude time plot in a logarithmic-time coordinate system after turning off the pulse (Fig. 14 (b)). The damping rate was observed to decrease from -27.33 to -31.53 s^{-1}. To elucidate the synergy effect on the pulse decay process, the phase plot was determined to examine whether the oscillation amplitude (p') was in phase with the gradient of amplitude (dp/dt). Fig. 15 (a) and (b) compare the corresponding phase diagrams of the acoustic pulse fluctuation growth. The helical curve beginning from the central point characterizes the elevated oscillations in the phase plot. Both initially begin with small-amplitude pressure disturbances. However, such disturbances rapidly increase into a steady oscillation in Fig. 15 (b) for 0.3 s. Fig. 15(c) and (d) show the phase diagrams of the acoustic pulse decay process. The helical curve begins from the outer border to the central point and characterizes the decay oscillations in the phase plot. It can be clearly seen that the pressure gradient gradually decreased to zero. This meant that the pressure oscillation periodically decayed to zero. Furthermore, the oscillation amplitude was dramatically reduced in the motor with the baffle. Therefore, the baffle accelerates the dissipation of such acoustic oscillations.

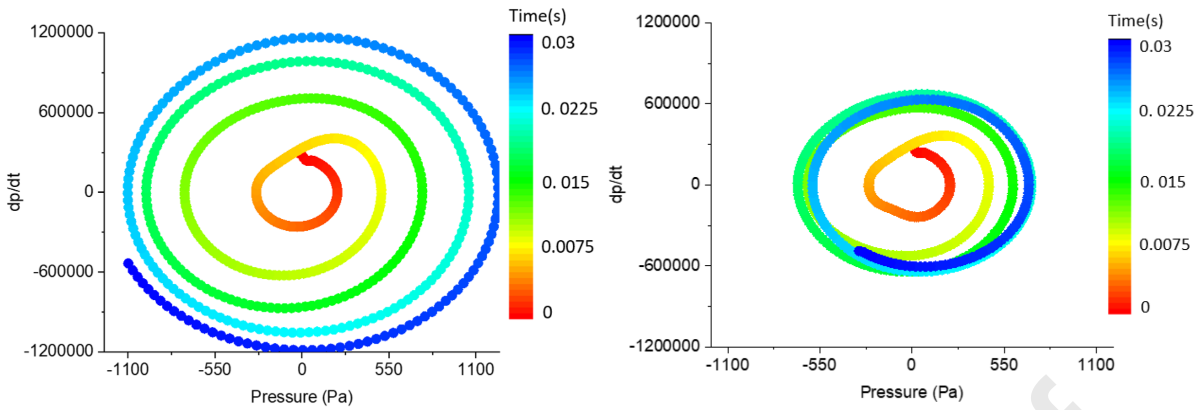

(a) Pulse growth (case 0) **(b) Pulse growth (case 4)**

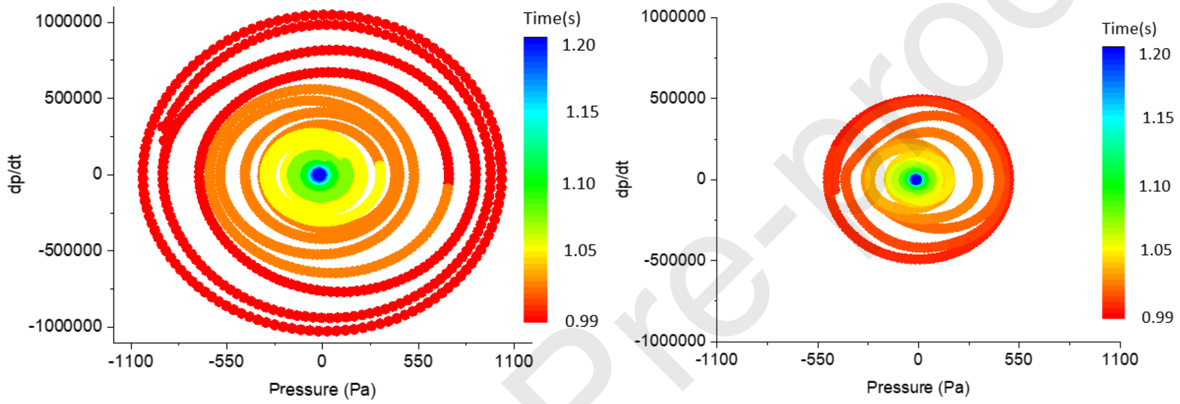

(c) Pulse decay (case 0) **(d) Pulse decay (case 4)**

Fig. 15 Comparison of phase diagrams

3.3 Damping Performances on Different Monitor Positions

The constructive damping responses at different positions of the baffle in the motor varied. To explore the axial position effect, we compared the growth rate and decay rate at different positions in the first half of the motor. According to the above-described data processing method, the comparisons of the growth and damping rates with various monitoring point positions are illustrated in Fig. 16. The lower growth rate and damping rate indicated a better suppression effect on the motor instability. The growth rate for case 0 was higher than that for case 4. The highest growth rate of approximately 43642 Pa/s was achieved at x/L= 1/16 for case 0. The growth rate is dependent on position owing to the acoustic pressure anti-node at the head end. In addition, when the monitors moved to the motor rear, the pressure growth rate of the trigger pulse increased slightly and then decreased in the position range from 2/16 to 5/16. The average growth rate decreases from 37339 to 23360 Pa/s owing to the baffle implementation in the motor. Therefore, the effect of the baffle on the trigger pulse growth rate is related to the monitor position.

Fig.16 (b) shows that the absolute damping rates of case 4 were higher than those of case 0. The damping rates of the motor without and with baffle were -27.33 and -31.53 s^{-1}, respectively. We observed that the damping rates of a certain motor remained almost the same for different sensor point positions. This indicated that the baffle can affect the overall acoustic cavity rather than being limited to the local area. Although the forcing pulses were imposed by the same mass flow rate, the initial amplitudes of the pulse were different after the pulse was cut off. The damping rate was also verified for all numerical scenarios and was observed to be independent of the initial amplitude of the pulse. The positive effect of the baffle was sufficient to change the damping capability of the motor. This was in good agreement with the results in Ref. [14]. The difference between cases 0 and 4 was primarily caused by the implementation of the baffle, which was the only structural improvement. The above-mentioned phenomenon is described to illustrate the damping mechanism of the baffle. This motivated further analysis of the effect of baffle geometry on the damping effect. The diameter and position were important parameters for further analyses. The following section describes the numerical data obtained from the head-end point.

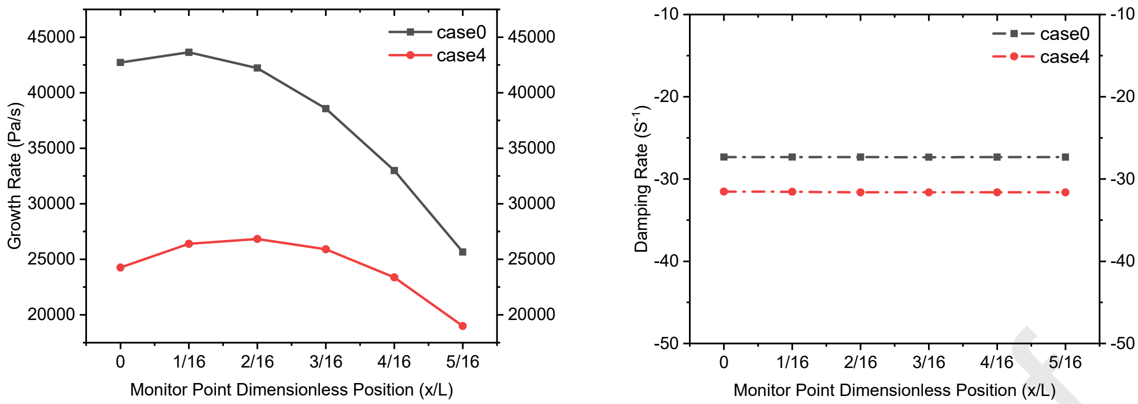

(a) Growth rate **(b) Damping rate**

Fig. 16 Comparisons of growth and damping rates on different monitor positions for the motors with (case 4) and without (case 0) a baffle

3.4 Effect of Baffle Location on Damping Performances

To explore the effect of the baffle location on the damping performance, we investigated acoustic pressure oscillations and related normalized acoustic energy levels in different baffle locations. As a pulse was triggered, acoustic pressure disturbances were initially generated with a small amplitude. The forced pulse resulted in an expected standing wave cycle with classical sine acoustic pressure fluctuations. Subsequently, it decayed to zero at an exponential rate. The full evolution of the acoustic disturbances is examined in this section. Fig. 17 shows the acoustic pressure oscillations (p') at the head-end point of the motor as the baffle location was set at four different axial locations (x/L). The pulsating pressure oscillations were zoomed. We observed that the amplitudes were dramatically narrowed in most cases.

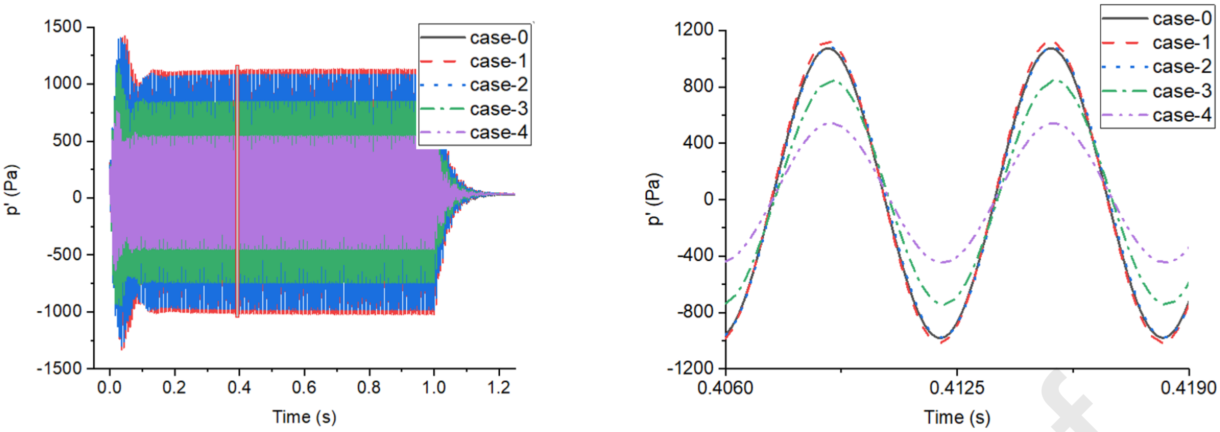

(a) Pressure evolution **(b) Zoom in view**

Fig. 17 Pulse response of motor with baffle at different locations.

Fig.18 shows the normalization of the acoustic energy and ratio variation with time. Acoustic energy increased gradually to different values in all cases. It developed more gradually in cases 3 and 4 of the motor with a damping baffle. However, in cases 1 and 2, acoustic energy increase faster than that in case 0. When the baffle was placed at x/L=1/2, the acoustic energy (E_a) reduced to approximately 45% of that in the motor without baffle. This confirmed that the acoustic pressure fluctuations were successfully suppressed from increasing into steady cycles.

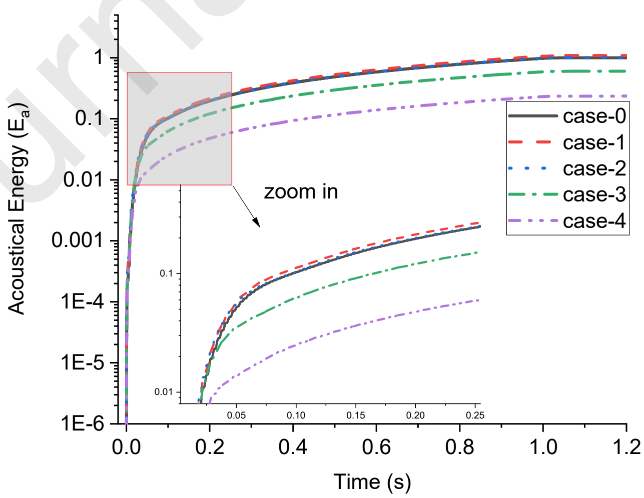

Fig. 18 Evolution of acoustic energy of motors with different baffle locations

Fig. 19 shows the effect of baffle on damping capability by the adjustments of locations in the motor. Baffle location has been correlated to the increasing the values of the growth and damping rates. To obtain these quantity values for various conditions, the location was varied from x/L = 1/16 to 1/2 with the same baffle (d/D=1/2) configuration. When the head-end baffle was moved from 1/16 to 1/8, the pressure growth rate increased slightly from 40961 to 42247 Pa/s, then decreased to 24255 Pa/s; the minimum value was 20000 Pa/s at the normalized location of x/L = 1/4. When the location of the baffle was less than 1/8, no apparent suppression on the acoustic oscillation was observed.

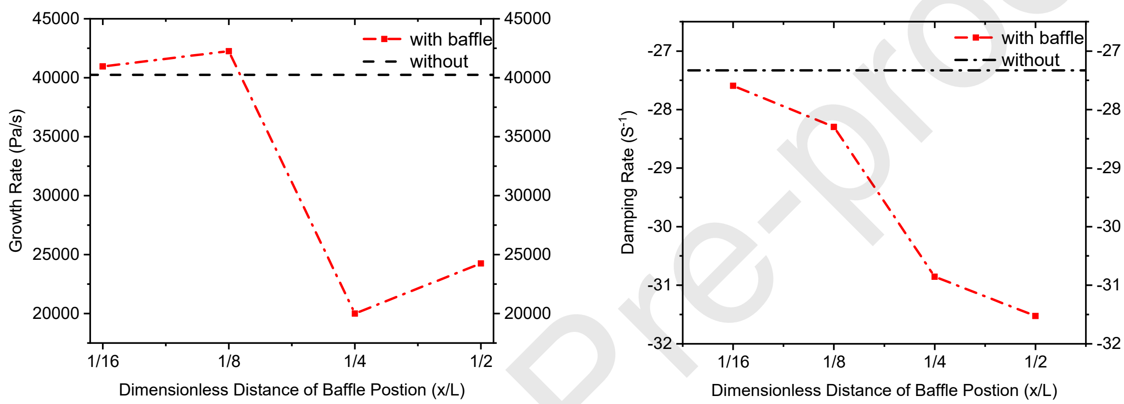

(a) Growth rate **(b) Damping rate**

Fig. 19 Effect of normalized baffle locations (*x/L*) on damping performance

As Fig. 19 (b) shows, the damping rates of motors with baffle were lower than that of case 0. When the baffle location moved from the head to the rear, the damping rate values decreased from -27.59 to -31.52 S^{-1}. The lowest damping rate was -31.52 S^{-1} in case 4. Regardless of the exact location of the baffle, there was a significant difference in the damping acoustic oscillations in the motor. The relative improvement in both the growth and damping rates with the baffle at x/L=1/2 was maintained at 51% and 15.3%, respectively, compared with the motors without a damping baffle. These results were in agreement with the finding in Ref. [44] that the axial acoustic oscillation can be suppressed if a baffle is located at the mid-point of the motor. For comparison, the damping rates were normalized. The normalized damping rates in Ref. [23] and in this study are compared in Fig. 20. The location dependence of the baffle on the damping ratio is only related to the slope in Fig. 20, and it is independent of the intercept. The results calculated in this paper are normalized and compared with the theoretical results in Ref. [23]. The slopes were nearly the same, which indicated that change discipline is similar. The damping rates changed nearly linearly with the variation in the baffle location. Considering both the suppression of pulse growth and the promotion of the pulse attenuation, the baffle had a favorable damping effect only when it was placed at the normalized axial location from 1/4 to 1/2. The theoretical calculation method in the reference can only evaluate the performance of the baffle in the cylinder motor with constant diameter and fails to consider the effects such as vortex dissipation. The selected motor in this paper has a gradual burning surface and a submerged nozzle, so the present result has somewhat deviated from the theoretical calculation. This is also the reason for us to explore the present numerical method. Therefore, this numerical method can also be effectively applied to the damping evaluation of complex configurations.

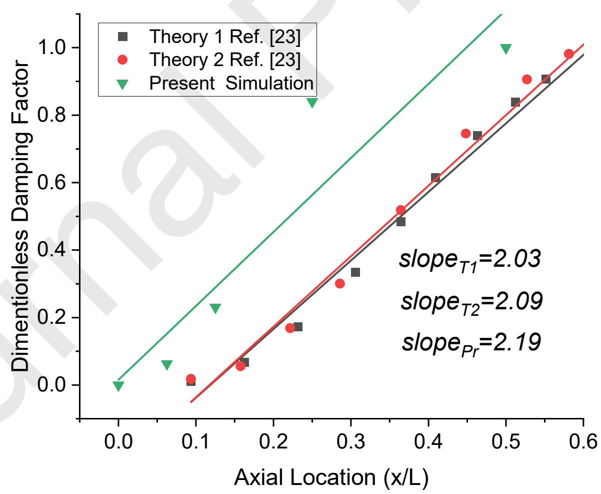

Fig. 20 Comparison of present simulation and theoretical results in Ref. [23]

3.5 Effect of Baffle Diameter on Damping Performances

We also confirmed that the baffle diameter is a dominant parameter affecting the suppression of acoustic instability. To explore the effect of baffle diameter on the damping performance, we investigated acoustic pressure oscillations and related normalized acoustic energy levels for different baffle diameters. The full evolution of acoustic disturbances with a pulse was the same as in the previous section. Fig. 21 shows the acoustic pressure oscillations (p') at the head end of the motor when the baffle location was 1/4, as baffles with five different diameters (*d/D)* were adopted. The evolution of all acoustic pressures increased with a peak value, decreased, and then "saturated" to a limit cycle. The acoustic modes changed significantly because of the installation of baffles with different diameters, and the amplitude of the acoustic oscillation cycle changed as well. Furthermore, the pulsating pressure oscillations and a zoom in view are shown in Fig. 21(b). The pressure amplitude of case 3 was lower than that of cases 5, 6, 7, and 8. In other words, a baffle with a smaller inner diameter suppresses acoustic oscillations well.

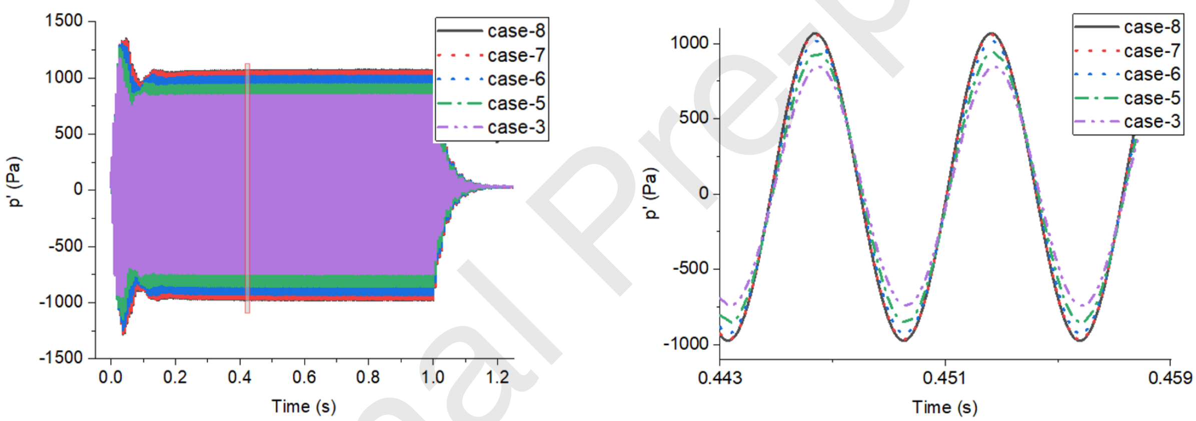

(b) Pressure evolution **(b) Zoom in view**

Fig. 21 Pulse response of motors with different diameters

Fig. 22 shows the normalization of the acoustic energy integral variation with time. Acoustic energy increased gradually to various levels in all cases. It developed more gradually in cases 3 and 5 of the motor with damping baffle. However, the acoustic energy of cases 7 and 8 remained at a same higher level. When the baffle was placed at x/L=1/4, the baffle in case 3 dampened more acoustic energy E_a.

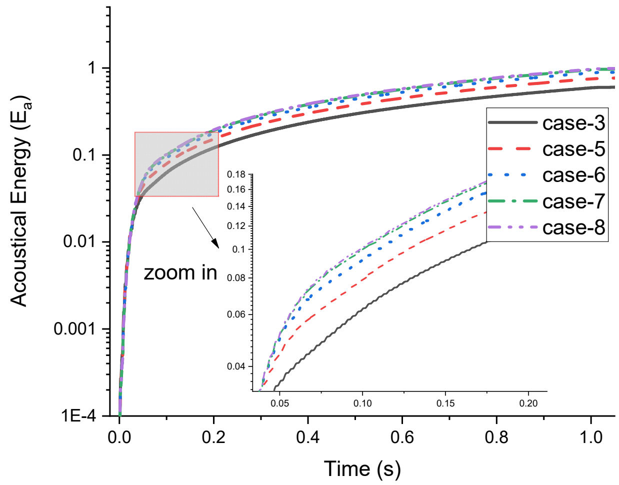

Fig. 22 Evolution of acoustic energy in motors with different baffle diameters

In this section, we examine the damping capability of the baffle when its diameter is adjusted. Fig. 23 shows the growth and damping rates for different diameters. If the baffle port diameter is sufficiently small, it may cause unnecessary performance losses. To balance the negative applications, this study did not adopt a diameter that was too small. The black dashed baseline denotes a motor without a baffle. It is shown that the growth rate in the motor with the baffle is relatively lower than that of the motor without a baffle. The baffle location was correlated to the value of the growth and damping rates. To obtain these quantity values for various conditions, the normalized diameter of the baffle was varied from 1/2 to 15/16, together with the same location (*x/L=1/4*) configuration. With a baffle-normalized diameter increased from 1/2 to 15/16, the pressure growth rate increased from 20000 to 42247 Pa/s, and then decreased at *d/D=7/8*. Fig. 23 (b) shows that the damping rates of motors with baffle were lower than the baseline. As the baffle diameter (*d/D*) increased, the values increased from -30.85 to -27.42 s^{-1}. The annular baffle with a smaller inner diameter was observed to be the geometric configuration to suppress combustion-excited acoustic oscillations. The baffle-induced improvement in the damping performance was attributed to the narrow traveling path of the acoustic wave front. This is the fundamental mechanism for explaining baffles. The lowest damping rate was -30.85 s^{-1}

with a diameter of 1/2 in case 3, when considering both the growth and damping rates of acoustic pressure oscillations. Although a smaller diameter has a better effect, an excessively small flow channel will affect the flow instability and motor performance. Hence, the motor with a baffle in case 3 was observed to be associated with a favorable damping effect. As the height of baffle (H) decreased (smaller inner diameter), the average and peak values of the turbulent viscosity ratio both increased. A more intense turbulent viscosity indicates that acoustic energy is easily converted into vortical energy and dissipated without significant acoustic regeneration [43]. Therefore, from the perspective of viscosity losses, this is an explanation of why a smaller diameter baffle is more effective.

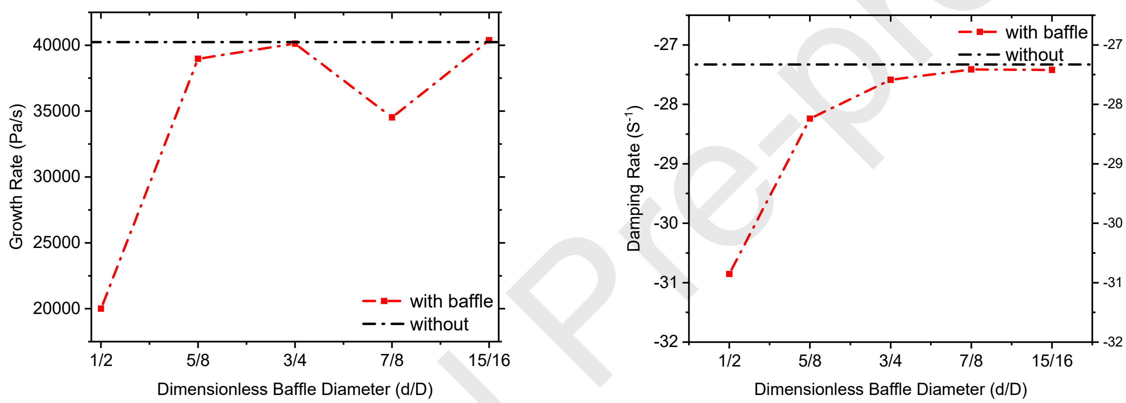

(a) Growth rate **(b) Damping rate**

Fig. 23 Effect of normalized diameter (d/D) on damping performance

4. Conclusions

In this study, 2D axisymmetric numerical investigations were conducted to quantitatively evaluate the damping performance of a baffle in a full-scale SRM. The growth and decay rates of acoustic oscillations for the SRM with and without a baffle were compared. The pulse response method was validated first using data available in the literature. Several numerical investigations were conducted to develop geometry design criteria to ensure the effectiveness of the baffle used to suppress combustion-excited acoustic oscillations in the SRM. The baffle implementation configurations were evaluated by the pulse attenuation method to obtain an optimum design. The key conclusions are summarized as follows.

- The acoustic growth rate, damping rate, and acoustic energy, as proposed in this paper, can be used to quantitatively evaluate the damping performance of the baffle on trigger pulse growth and pulse attenuation.
- The most apparent effect of the baffle on trigger pulse growth was observed to occur at the head-end (1/16 the length) of the SRM. The damping rates of the SRM without and with the baffle were observed to be -27.33 to-31.53 s^{-1}, respectively. The damping rates of the SRM were independent of the monitoring point positions.
- The baffle can be employed to suppress combustion-excited acoustic oscillations only when it is placed at a normalized axial location from 1/4 to 1/2. It has been confirmed that applying the damper at x/L=1/2 results in 51% and 15.3% relative improvement in the growth and damping rates, respectively, compared with those in a SRM without a baffle.
- The geometric configuration of the annular baffle with a smaller inner diameter effectively suppresses combustion-excited acoustic oscillations. The lowest damping rate is -30.85 s-1 for the baffle with a diameter of d/D=1/2, which was observed to be associated with a favorable damping effect.

Conflict of interest statement

The authors declared that they have no conflicts of interest to this work.

Acknowledgments

This work was funded by the International Graduate Exchange Program of Beijing Institute of Technology and supported by the University of Canterbury under grant number 452STUPDZ. Lei Han would like to thank the University of Canterbury for hosting his PhD exchange studentship in the group of Dr. Dan Zhao.

References

[1] M. Laureti, G. Rossi, B. Favini, Aeroacoustics of Aft-Finocyl Solid Rocket Motors, 2018 Joint Propulsion Conference, 2018.

[2] F. Blomshield, Lessons Learned In Solid Rocket Combustion Instability, 43rd AIAA/ASME/SAE/ASEE Joint Propulsion Conference & Exhibit, 2007.

[3] J. Anthoine, M. Lema, Comparison of Different Passive Control Solutions for Reducing SRM Pressure Oscillations Using Cold Flow Experiments, 44th AIAA/ASME/SAE/ASEE Joint Propulsion Conference & Exhibit, 2008.

[4] B.B. Sun, S.P. Li, W.X. Su, J.W. Li, N.F. Wang, Effects of gas temperature on nozzle damping experiments on cold-flow rocket motors, Acta Astronautica, 126 (2016) 18-26.

[5] S. Oh, Y. Shin, Y. Kim, Stabilization effects of perforated plates on the combustion instability in a lean premixed combustor, Applied Thermal Engineering, 107 (2016) 508-515.

[6] Y. Fabignon, J. Dupays, G. Avalon, F. Vuillot, N. Lupoglazoff, G. Casalis, M. Prévost, Instabilities and pressure oscillations in solid rocket motors, Aerospace Science and Technology, 7 (2003) 191-200.

[7] E. Cavallini, B. Favini, M. Castelli, A. Neri, VEGA Launch Vehicle Dynamic Loads due to Solid Propulsion Ignition Transients and Pressure Oscillations, 52nd AIAA/SAE/ASEE Joint Propulsion Conference, 2016.

[8] L. Hirschberg, T. Schuller, C.F. Schram, J. Collinet, Lumped model for vortex sound in large Solid Rocket Motors, 2018 AIAA/CEAS Aeroacoustics Conference, 2018.

[9] S. Gallier, M. Prevost, J. Hijlkema, M. Roumy, Effects of Cavity on Thrust Oscillations in Subscale Solid Rocket Motors, 45th AIAA/ASME/SAE/ASEE Joint Propulsion Conference & Exhibit, 2009.

[10] V. Ferretti, B. Favini, E. Cavallini, F. Serraglia, M. Di Giacinto, Numerical simulations of acoustic resonance of Solid Rocket Motor, 46th AIAA/ASME/SAE/ASEE Joint Propulsion Conference & Exhibit, 2010.

[11] A. Di Mascio, E. Cavallini, B. Favini, A. Neri, Numerical Simulation of 3D Unsteady Flowfield in Aft-Finocyl Solid Rocket Motor, 50th AIAA/ASME/SAE/ASEE Joint Propulsion Conference, 2014.

[12] D. Zhao, X.Y. Li, A review of acoustic dampers applied to combustion chambers in aerospace industry, Progress in Aerospace Sciences, 74 (2015) 114-130.

[13] S. Jo, Y. Choi, H.J. Kim, Evaluation of the damping capacity according to the geometric and the number of resonator with thermal environment using a Rijke tube, Aerospace Science and Technology, 88 (2019) 1-8.

[14] A. Javed, D. Chakraborty, Damping Coefficient Prediction of Solid Rocket Motor Nozzle Using Computational Fluid Dynamics, Journal of Propulsion and Power, 30 (2014) 19-23.

[15] D. Mason, R. Morstadt, S. Cannon, E. Gross, D. Nielsen, Pressure Oscillations and Structural Vibrations in Space Shuttle RSRM and ETM-3 Motors, (2004).

[16] S. Ji, B. Wang, D. Zhao, Numerical analysis on combustion instabilities in end-burning-grain solid rocket motors utilizing pressure-coupled response functions, Aerospace Science and Technology, 98 (2020) 105701.

[17] T. Cai, S.M. Becker, F. Cao, B. Wang, A. Tang, J. Fu, L. Han, Y. Sun, D. Zhao, NO emission performance assessment on a perforated plate-implemented premixed ammonia-oxygen micro-combustion system, Chem. Eng. J., (2020) 128033.

[18] D. Zhao, E. Gutmark, A. Reinecke, Mitigating self-excited flame pulsating and thermoacoustic oscillations using perforated liners, Science Bulletin, 64 (2019) 941-952.

[19] C.H. Sohn, J.H. Park, A comparative study on acoustic damping induced by half-wave, quarter-wave, and Helmholtz resonators, Aerospace Science and Technology, 15 (2011) 606-614.

[20] G. Wu, Z. Lu, X. Xu, W. Pan, W. Wu, J. Li, J. Ci, Numerical investigation of aeroacoustics damping performance of a Helmholtz resonator: Effects of geometry, grazing and bias flow, Aerospace Science and Technology, 86 (2019) 191-203.
[21] Le. Helley, System and method of controlling pressure oscillations of hydrodynamic origin for a solid propellant thruster, AVIO, United States, 2006.
[22] N.P. Yadav, A. Kushari, Passive control of premixed lifted flame in a dump combustor, Fuel, 93 (2012) 67-74.
[23] C.L. Oberg, W.G. Haymes, Solid propellant combustion instability suppression devices, AIAA/SAE 8th Joint Propulsion Specialist ConferenceNew Orleans, Louisiana, 1972.
[24] F.G. Buffum, G.L. Dehority, R.O. Slates, E.W. Price, Acoustic attenuation experiments on subscale, cold-flow rocket motors, AIAA Journal, 5 (1967) 272-280.
[25] F. Stella, F. Paglia, Pressure oscillations in solid rocket motors: Numerical study, Aerospace Science and Technology, 15 (2011) 53-59.
[26] E. Cavallini, B. Favini, A. Neri, Motor Scale and Propellant Geometry Effects on Pressure Oscillations in Aft-Finocyl Solid Rocket Motors, 52nd AIAA/SAE/ASEE Joint Propulsion Conference, 2016.
[27] D. Zhang, S. Cheng, F. Xu, Y. Hu, H. Li, Study on nonlinear vibration of simplified solid rocket motor model, Aerospace Science and Technology, 93 (2019) 105302.
[28] L. Chen, Y. Gao, D. Wang, Q. Zou, S. Zhang, Numerical simulation on acoustic mode and pressure-oscillation decay in finocyl- and axil-grain combustion chambers, Aerospace Science and Technology, 107 (2020) 106351.
[29] Y. Yun, J. Seo, K. Park, J. Huh, J. Lim, S. Kwon, Integration validation of key components for small sounding rockets, Aerospace Science and Technology, 100 (2020) 105823.
[30] D. Wang, Y. Yang, W. Fan, X. Li, Y. Gao, Simulation of pressure oscillations in a combustion chamber under periodic inlet disturbances, Acta Astronautica, 152 (2018) 859-871.
[31] ANSYS Inc. Fluent theory guide. Version 18.0. vols. 3 and 4. Canonsburg: ANSYS Inc., 2017.
[32] R.A. Ahmad, Convective Heat Transfer in the Reusable Solid Rocket Motor of the Space Transportation System, Heat Transfer Engineering, 26 (2005) 30-45.
[33] L. Peng, G. He, J. Li, L. Wang, F. Qin, Effect of combustion gas mass flow rate on carbon/carbon composite nozzle ablation in a solid rocket motor, Carbon, 50 (2012) 1554-1562.
[34] A. Scarpato, Linear and nonlinear analysis of the acoustic response of perforated plates, PhD Thesis, École Centrale Paris, 2014.
[35] J.M. Wicker, M.W. Yoon, V. Yang, Linear and non-linear pressure oscillations in baffled combustion chambers, Journal of Sound and Vibration, 184 (1995) 141-171.
[36] X. Jing, X. Sun, Effect of Plate Thickness on Impedance of Perforated Plates with Bias Flow, AIAA Journal, 38 (2000) 1573-1578.
[37] W. Su, N. Wang, J. Li, Y. Zhao, M. Yan, Numerical Research on The Nozzle Damping Effect by A Wave Attenuation Method, Defence Technology, 9 (2013) 162-166.
[38] E. Gullaud, F. Nicoud, Effect of Perforated Plates on the Acoustics of Annular Combustors, AIAA Journal, 50 (2012) 2629-2642.
[39] D. Zhao, Y. Guan, A. Reinecke, Characterizing hydrogen-fuelled pulsating combustion on thermodynamic properties of a combustor, Communications Physics, 2 (2019).
[40] A. Flatau, W. Vanmoorhem, Prediction of vortex shedding responses in segmented solid rocket motors, 26th Joint Propulsion Conference, 1990.
[41] P. Roache, Error Bars for CFD, 2003.
[42] D.W. Bechert, Sound absorption caused by vorticity shedding, demonstrated with a jet flow, Journal of Sound and Vibration, 70 (1980) 389-405.
[43] A. Cummings, Acoustic nonlinearities and power losses at orifices, AIAA Journal, 22 (1984) 786-792.
[44] T. Koreki, I. Aoki, K. Shirota, Y. Toda, An experimental study on oscillatory combustion in solid propellant motor, AIAA/SAE 11th Propulsion ConferenceAnaheim, California, 1975.

Declaration of interests

☒ The authors declare that they have no known competing financial interests or personal relationships that could have appeared to influence the work reported in this paper.

☐The authors declare the following financial interests/personal relationships which may be considered as potential competing interests: